Optimizing composition of $Pb(Bi_{1-x}Sb_x)_2Te_4$ topological insulator to achieve a bulk-insulating state

Yuya Hattori, Yuki Tokumoto,* and Keiichi Edagawa
Institute of Industrial Science, The University of Tokyo, Komaba, Meguro-ku, Tokyo 153-8505, Japan
(Received 4 August 2017; revised manuscript received 16 November 2017; published 7 December 2017)

A series of $Pb(Bi_{1-x}Sb_x)_2Te_4$ topological-insulator crystals with various Sb molar ratios x was fabricated, and a systematic study of their transport properties was performed, aiming at realizing enhanced bulk insulation in this system. Hall-effect measurements showed that n- to p-type transition in bulk conduction occurred at $x \approx 0.80$. Semiconducting behavior with a negative temperature coefficient of resistivity was observed with resistivity values as high as 180 mΩ cm at 2 K around the transition composition. The conduction mechanism in the semiconducting samples is discussed in relation to an impurity band formed within the bandgap.

DOI: 10.1103/PhysRevMaterials.1.074201

I. INTRODUCTION

Topological insulators (TIs) are a new class of quantum matter, characterized by a bulk bandgap and gapless edge or surface states that host helically spin-polarized Dirac fermions [1]. These gapless states are protected by time reversal symmetry, and therefore they are robust against disorder scattering. The experimental demonstration of two-dimensional (2D) [2] and three-dimensional (3D) [3] TIs has generated much interest from both fundamental and technological points of view, and these exotic states of matter have ever since been studied extensively.

Currently, one of the most urgent tasks in the field of 3D TIs is to achieve a bulk-insulating state, which is a prerequisite for the study of characteristic surface-transport phenomena by spin-polarized Dirac fermions. In general, bulk-insulating TIs are hard to realize because of their narrow bandgaps and charge carriers due to intrinsic crystalline lattice defects such as vacancies and antisites [4]. Though TIs have so far been realized in many systems, only a limited number of these have exhibited bulk-insulating behavior [5], including some of the most intensively studied $(Bi,Sb)_2(S,Se,Te)_3$ tetradymites [6–13].

Bi_2Se_3 and Bi_2Te_3 tetradymites have simple surface states with a single Dirac cone in the Brillouin zone, hence they have been widely considered to be appropriate platforms for studying the topological surface transport [6]. However, near-stoichiometric Bi_2Se_3 and Bi_2Te_3 are usually highly metallic due to charge carriers created by lattice defects. In 2010, Qu *et al.* [7] fabricated nonmetallic crystals of Bi_2Te_3 by fine tuning the off-stoichiometry composition, and measured the surface quantum transport. However, the bulk resistivity was still low (∼12 mΩ cm), and the surface contribution to the total conduction did not exceed 0.3%. Subsequently, many efforts were made to reduce the bulk conductivity by tuning the chemical composition and/or doping in $(Bi,Sb)_2(S,Se,Te)_3$ tetradymites [8–13]. As a result, in $Bi_{1.5}Sb_{0.5}Te_{1.7}Se_{1.3}$, surface contribution as high as 70% to the total conductance was achieved [13].

Recently, a homologous series of layered chalcogenides, $(AX)_n(B_2X_3)_m$ (A = Pb,Sn,Ge; B = Bi,Sb; and X = S,Se,Te) have been theoretically revealed as 3D TIs [14–17]. They are expected to offer greater chemical and material tunabilities than the binary tetradymite family [18]. In $PbBi_2Te_4$, a member of the Pb-based layered chalcogenides, a single Dirac cone has been observed by angle-resolved photoemission spectroscopy (ARPES) [19,20]. Energy dispersion curves obtained by ARPES measurements revealed that $PbBi_2Te_4$ has the highest surface carrier density of all the 3D TIs studied so far [20]. Furthermore, it has been theoretically shown that $PbBi_2Te_4$ has a more isotropic Dirac cone than related binary TIs such as Bi_2Te_3 [15,17]. Here, such an isotropic Dirac cone should work for suppressing the scattering of surface electrons [21]. Thus, $PbBi_2Te_4$ can be considered one of the promising candidates for future spintronics material with a large spin current density.

In addition to the potential advantages described above, we should note that the Z_2 topological invariants for $PbBi_2Te_4$ have been determined to be $(\nu_0;\nu_1\nu_2\nu_3) = (1;111)$ [14,15,20]. According to the classification by Slager *et al.* [22], this phase can be indexed as $T - r\bar{3}_Z$, belonging to the class of "translationally active" states, in which 1D gapless states could form along crystalline dislocations [23,24]. In contrast, most of the TIs discovered so far, including $(Bi,Sb)_2(S,Se,Te)_3$ tetradymites, are of the class of Γ states with the invariants (1;000), where no 1D gapless states along the dislocations can be realized. Tretiakov *et al.* pointed out the possibility of thermoelectric applications of such conductive dislocations [25]. Recently, conductivity measurements on plastically deformed Bi-Sb TIs showed excess conductivity owing to dislocation conduction [26].

Although a surface Dirac cone was observed by ARPES in $PbBi_2Te_4$ [19,20], experimental studies of its surface transport properties have not yet been reported, owing to a lack of bulk-insulating crystals; bulk resistivity is as low as 0.5 mΩ cm at 20 K due to carriers originating from lattice defects [27]. ARPES studies by Souma *et al.* [19] have shown that the chemical potential can be tuned by Sb substitution for Bi in $PbBi_2Te_4$; whereas $PbBi_2Te_4$ and $Pb(Bi_{0.6}Sb_{0.4})_2Te_4$ are n-type materials, $PbSb_2Te_4$ is a p-type one. In view of this, we fabricated a series of $Pb(Bi_{1-x}Sb_x)_2Te_4$ crystals by varying x, and systematically studied their transport properties, with the objective of realizing enhanced bulk insulation in this system.

II. EXPERIMENTAL PROCEDURES

$Pb(Bi_{1-x}Sb_x)_2Te_4$ crystals with varying x were grown by the Bridgman method. First, a mixture of high-purity (6N) Pb, Bi, Sb, and Te elements, in the molar ratio

*Corresponding author: tokumoto@iis.u-tokyo.ac.jp

 ©2017 American Physical Society

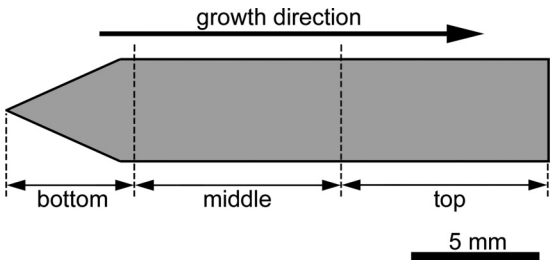

FIG. 1. A schematic of the shape of the ingot.

of Pb : Bi : Sb : Te = 1 : (2 − 2x) : 2x : 4, was sealed in an evacuated quartz ampoule. Then, they were melted and homogenized at 800 °C, followed by water quenching. Subsequently, the ingots were subjected to the Bridgman method for crystal growth. The ampoule translation speed was set at 2–3 mm/h. The temperature gradient in the furnace was approximately 25 °C/cm around the position of the liquidus temperature. The phase constitution and composition of the grown crystals were investigated by an electron probe microanalyzer (EPMA). For quantitative composition analyses, a melt-spun $PbBiSbTe_4$ sample produced by a single-roller method was used as a standard for ZAF conversion from the intensities of Pb $M\alpha_1$, Bi $M\alpha_1$, Sb $L\alpha_1$, and Te $L\alpha_1$ to concentrations. The crystalline phases were identified by powder x-ray diffraction (XRD) using Cu $K\alpha$ radiation.

The $Pb(Bi_{1-x}Sb_x)_2Te_4$ phase with a rhombohedral crystal structure has a basal cleavage on the (111) plane. Single crystals of the phase were retrieved from a middle part of the ingot by breaking the ingot along the cleavage planes for electrical transport measurements. The sample size was approximately $x \times y \times z = 2.0 \times 1.0 \times 0.15$ mm^3, where the z direction was parallel to the [111] direction and the current direction was along the x direction. Electrical transport measurements were conducted by a six-probe method using a physical property measurement system (PPMS). Ohmic electrical contacts were fabricated using a room-temperature cured silver paste. Resistivity was measured in the temperature range between 2 and 300 K. Carrier densities were evaluated by measuring the Hall effect at 2 K, assuming single-carrier conduction. The magnetoresistance (MR) was measured at various temperatures in an out-of-plane magnetic field (parallel to the z direction) up to 9 T.

III. RESULTS AND DISCUSSION

A. Crystal growth

Figure 1 shows a schematic of the shape of the ingot. As described in detail below, in view of the constitution of phases observed by EPMA and XRD measurements, the sample can be divided into three different regions: The bottom region ($r < 5$ mm), the middle region ($5 < r < 13$ mm), and the top region ($r > 13$ mm), where r denotes the distance from the bottom end of the sample. EPMA elemental mappings using Pb $M\alpha_1$ and XRD patterns of the three regions in the sample with the nominal composition $Pb(Bi_{1-x}Sb_x)_2Te_4$ (x = 0.60) are presented in Figs. 2(a)–2(c) and in Figs. 3(a)–3(c), respectively.

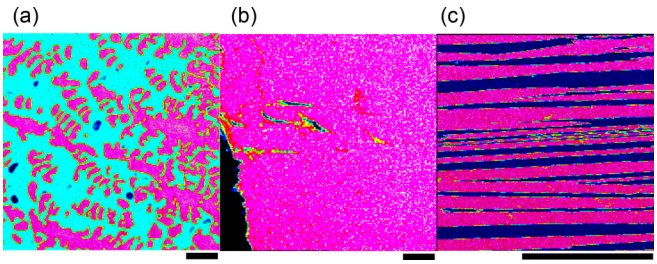

FIG. 2. EPMA Pb elemental mappings for the bottom (a), middle (b), and top (c) regions of the ingot with the nominal composition $Pb(Bi_{1-x}Sb_x)_2Te_4$ ($x = 0.6$). Scale bars represent 300 μm.

In the Pb mapping from the bottom region [Fig. 2(a)], two phase regions are observed: a light blue matrix and pink dendritic areas. Here, several blue spots are also observed but they have been identified as dents on the sample surface. EPMA measurements showed that the compositions of the light blue and pink regions are $Pb_{12.0}(Bi,Sb)_{29.3}Te_{58.7}$ and $Pb_{38.3}(Bi,Sb)_{7.3}Te_{54.4}$, respectively. The XRD spectrum measured for the bottom region of the sample is presented in Fig. 3(a), in which two phases are identified: cubic PbTe and rhombohedral $Pb(Bi_{1-x}Sb_x)_2Te_4$. The XRD result, together with the results of EPMA, indicates that the light blue region in Fig. 2(a) corresponds to the rhombohedral $Pb(Bi_{1-x}Sb_x)_2Te_4$ phase, whereas the pink dendritic region corresponds to the cubic PbTe phase containing Bi and Sb as solute atoms.

In Fig. 2(b), the Pb mapping from the middle region of the sample is shown. Here, the entire region is pink, indicating the Pb concentration is almost constant in this region. There appear to be several blue regions inside, but they are dents on the sample surface. EPMA measurements showed that the composition in this region is $Pb_{12.6}(Bi,Sb)_{30.6}Te_{56.8}$, suggesting that the phase formed is rhombohedral $Pb(Bi_{1-x}Sb_x)_2Te_4$. In fact, in the XRD pattern of Fig. 3(b) measured for this region, all the peaks could be indexed as the rhombohedral

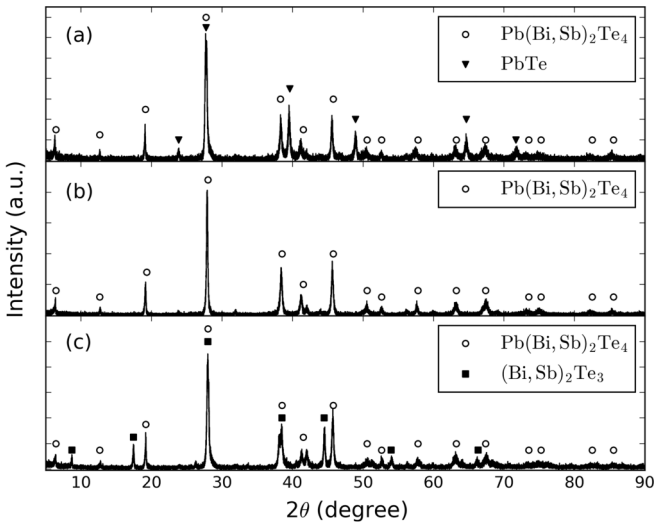

FIG. 3. Powder XRD patterns of the bottom (a), middle (b), and top (c) regions of the ingot with the nominal composition $Pb(Bi_{1-x}Sb_x)_2Te_4$ ($x = 0.6$).

$Pb(Bi_{1-x}Sb_x)_2Te_4$ phase. We confirmed that the entire middle region shown in Fig. 1 consists of a single phase. However, this region was not entirely a single crystal but consisted of several millimeter-sized crystal grains. In the middle region, a slight compositional variation was detected by detailed compositional analyses by EPMA; the compositional ratio of Sb to (Bi + Sb), i.e., x in $Pb(Bi_{1-x}Sb_x)_2Te_4$ changed linearly from 0.580 ± 0.005 at the bottom of the middle part to 0.595 ± 0.005 at the top of this part.

Figure 2(c) shows the Pb mapping of the top region of the sample shown in Fig. 1. A lamellar structure of the pink and blue regions is observed, which is typical of a eutectic structure. The compositions of the pink and blue regions are revealed by EPMA to be $Pb_{10.9}(Bi,Sb)_{29.5}Te_{59.6}$ and $Pb_{1.5}(Bi,Sb)_{36.7}Te_{61.8}$, respectively. The XRD pattern of the top region of the sample is presented in Fig. 3(c), in which two phases are identified: rhombohedral $Pb(Bi_{1-x}Sb_x)_2Te_4$ and $(Bi,Sb)_2Te_3$ phases, corresponding to the pink and blue regions in Fig. 2(c), respectively. Similar results of the phase constitution to those presented in Figs. 2(a)–2(c) and 3(a)–3(c) were obtained for all the samples with the nominal composition $x = 0.6$–0.9.

The phase constitution revealed by EPMA and XRD analyses is consistent with the phase diagram of the pseudobinary system $PbTe-Sb_2Te_3$ reported by Shelimova *et al.* [28]. According to the phase diagram, crystallization is expected to proceed as follows:

(i) Primary crystallization of PbTe from liquid.
(ii) Peritectic reaction: PbTe + liquid → $Pb(Bi,Sb)_2Te_4$.
(iii) Growth of $Pb(Bi,Sb)_2Te_4$.
(iv) Eutectic reaction: liquid → $Pb(Bi,Sb)_2Te_4$ + $(Bi,Sb)_2Te_3$.

The phase constitution observed in our sample is consistent with the above process. That is, the bottom region of the sample consists of PbTe and $Pb(Bi,Sb)_2Te_4$, which should be formed in the initial stages of the crystallization process, the middle region consists entirely of $Pb(Bi,Sb)_2Te_4$ expected to grow in the middle stage of the process, and the top region has a lamellar structure of $Pb(Bi,Sb)_2Te_4$ and $(Bi,Sb)_2Te_3$, which should be formed by the eutectic reaction expected in the final stage.

B. Electrical resistivity

Figure 4(a) shows the temperature dependence of the electrical resistivities of nine $Pb(Bi_{1-x}Sb_x)_2Te_4$ samples. In Fig. 4(b), the four samples that showed low resistivities are presented with an enlarged y scale for clarity. Table I presents the x values for the nominal composition and those evaluated by EPMA. The difference between the nominal and the evaluated x values is $\Delta x \leqslant 0.02$. In Figs. 4(a) and 4(b), the resistivities of samples D, E, G, and H indicate semiconducting characteristics with a negative temperature coefficient, whereas the others more or less exhibit metallic behavior with a positive temperature coefficient. In Fig. 5, the resistivities at 2 K are plotted against the evaluated x, where the blue and red circles are assigned to the negative and positive carrier types, respectively, revealed by Hall-effect measurements. The negative-to-positive transition occurs at certain composition in the range $x = 0.79-0.80$, and the compositions of samples D, E, G, and H, which exhibited semiconducting behavior

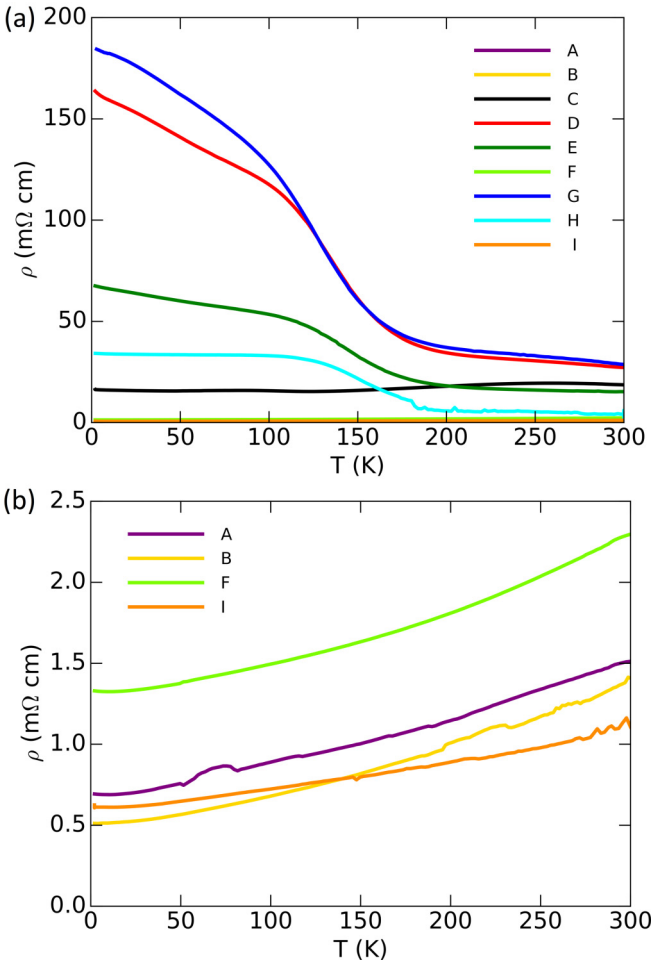

FIG. 4. (a) Temperature dependence of the electrical resistivity for nine samples of $Pb(Bi_{1-x}Sb_x)_2Te_4$ (see Table I). (b) That of the four samples showing low resistivities are presented with an enlarged y scale for clarity.

with large resistivities at 2 K, are close to the transition composition.

Of the nine samples (Table I), sample G showed the highest resistivity: $\rho \approx 180$ mΩ cm at 2 K. For this sample, the Hall coefficient was evaluated to be 3.6 cm^3/C at 2 K, leading to a carrier density of 1.7×10^{18} cm^{-3}. Pan *et al.* [27] reported a resistivity of 0.5 mΩ cm and carrier density

TABLE I. x values of $Pb(Bi_{1-x}Sb_x)_2Te_4$ samples for resistivity measurements: nominal x and that evaluated by EPMA.

Sample	Nominal x	Evaluated x
A	0.60	0.59 ± 0.01
B	0.70	0.72 ± 0.01
C	0.78	0.79 ± 0.01
D	0.79	0.791 ± 0.003
E	0.79	0.791 ± 0.003
F	0.80	0.80 ± 0.01
G	0.79	0.801 ± 0.004
H	0.80	0.803 ± 0.005
I	0.90	0.895 ± 0.01

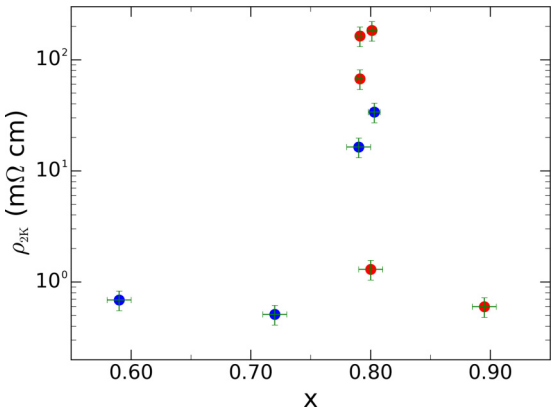

FIG. 5. Resistivity at 2 K (ρ_{2K}) plotted against the x values evaluated by EPMA, where the blue and red circles are assigned to the negative and positive carrier types, respectively, revealed by Hall-effect measurements.

of 2.2×10^{20} cm^{-3} for the ternary $PbBi_2Te_4$ phase at 20 K. Those of the ternary $PbSb_2Te_4$ phase were reported by Shelimova *et al.* [29] to be 0.18 mΩ cm and 1.0×10^{20} cm^{-3}, respectively, at 80 K. The resistivity and carrier density of sample G are higher and lower, respectively, than those of the ternary phases by two to three orders of magnitude.

With regard to the most intensively studied TIs of $(Bi,Sb)_2(Se,Te)_3$ tetradymites, many efforts have ever been made to achieve a bulk-insulating state, as mentioned in Sec. I. In early works, the samples of binary Bi_2Se_3 and Bi_2Te_3 mostly exhibited a metallic behavior with a positive temperature coefficient in resistivity, where the resistivity values were as low as ∼1 mΩ cm. In 2010, Qu *et al.* [7] succeeded in obtaining nonmetallic crystals of Bi_2Te_3 by fine tuning the off-stoichiometry composition, and reported the observation of Shubnikov–de Haas (SdH) oscillations arising from the surface conduction. Here, the resistivity value reported was 12 mΩ cm at 4 K, and the surface contribution to the total conductance was estimated to be only 0.3% for a sample with thickness of 0.14 mm. Subsequently, slightly off-stoichiometric Bi_2Te_2Se crystals were reported to exhibit high resistivity of ∼1 Ω cm, which enabled precise measurements of surface SdH oscillations [8]. Here, the surface contribution to the total conductance was estimated to be 6% for a sample with thickness of 0.26 mm, much improved from the binary Bi_2Te_3 crystals by Qu *et al.* [7]. After that, in quaternary $Bi_{1.5}Sb_{0.5}Te_{1.7}Se_{1.3}$, surface-dominant transport with surface contribution up to 70% was achieved in thin samples with thickness of $\leqslant 10$ μm. [13] Assuming that the surface conductivity in our $Pb(Bi_{1-x}Sb_x)_2Te_4$ crystals is comparable with those in the above-mentioned $(Bi,Sb)_2(Se,Te)_3$ ones, the surface contribution to the total conductance can be estimated to be 2−4% for our most resistive sample (sample thickness: 0.14 mm). If we reduce the sample thickness down to 10 μm, the surface contribution should go up to 20−40%. These facts indicate that our crystals should be available for the study of surface transport properties.

ARPES experiments were conducted for $Pb(Bi_{1-x}Sb_x)_2Te_4$ ($0 \leqslant x \leqslant 1$) by Souma *et al.* [19]. The bandgap was estimated to be $E_g \approx 0.2$ eV, which is slightly larger than that estimated

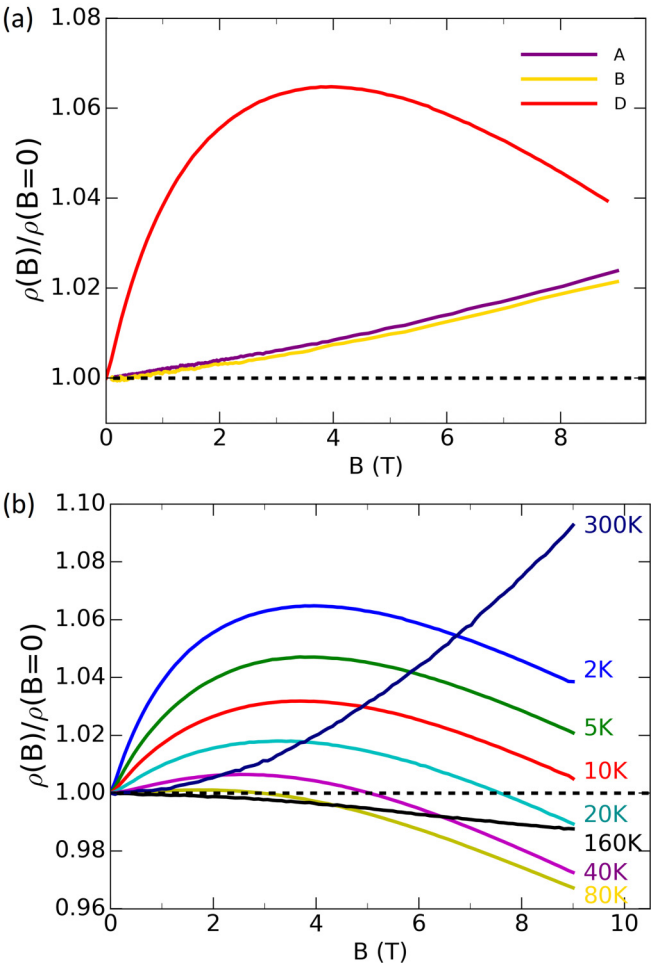

FIG. 6. (a) Magnetoresistances of samples A, B, and D measured at 2 K. (b) Magnetoresistances of sample D, measured at various temperatures.

by the band calculations [14,15] ($E_g = 0.1-0.15$ eV). Shift of the chemical potential in a rigid-band manner was observed with changing x. The chemical potential was located at ∼0.25 and ∼0.1 eV above the bottom of the conduction band for $x = 0$ and 0.4, respectively, whereas it was positioned at ∼0.05 eV below the top of the valence band for $x = 1.0$. That is, $PbBi_2Te_4$ and $Pb(Bi_{0.6}Sb_{0.4})_2Te_4$ are n-type degenerate semiconductors and $PbSb_2Te_4$ is a p-type one. In our experiments, the n-to-p transition was observed at $x \approx 0.80$, which is consistent with the ARPES results. In addition, our ρ_{2K} data (Fig. 5) suggest that μ traverses the gap of ∼0.2 eV in a narrow composition range around $x \approx 0.80$.

C. Magnetoresistance

Figure 6(a) shows the MR [$\rho(B)/\rho(B = 0)$] curves of some of the metallic samples (A and B) and that of a semiconducting sample (D), measured at 2 K. The metallic samples show positive MR roughly with B^2 dependence, which is often observed for conventional metals. The semiconducting sample also exhibits a positive MR, but its B dependence is qualitatively different from that of the metallic samples. The MR of sample D shows a rapid increase in the low-B region,

reaches a maximum at around 4 T, and then, decreases in the higher B region. The rapid MR increase in the low-B region can be interpreted as a weak antilocalization (WAL) behavior, a characteristic of strong spin-orbit coupling systems [30,31]. On the other hand, the MR decrease in the higher B region is in accordance with a weak localization (WL) behavior [30,31].

Figure 6(b) shows the MR curves of sample D, measured at different temperatures, in which a systematic change is observed. Upon increasing the temperature from 2 to 80 K, the slope of the curve in the low-B region becomes smaller, rendering the MR maximum smaller. As for the MR value at $B = 9$ T, it decreases from 1.04 at 2 K to 0.97 at 80 K, begins to increase at this temperature, and increases up to 1.09 at 300 K. The MR curve at 300 K shows clear B^2 behavior typical of conventional metals. These behaviors will be analyzed in detail in the following subsection.

D. Transport mechanism

In this subsection, we discuss the transport mechanism in the semiconducting samples. In Fig. 7(a), the Arrhenius plots of $\rho(T)$ data for the three most resistive samples (G, D, and E) in Fig. 4(a) are presented, where activated temperature dependence is seen in an intermediate temperature range around 150 K. The excitation energies evaluated are $\Delta = 31, 32$, and 34 meV for G, D, and E, respectively, which are much smaller than the bandgap ($E_g \approx 0.2$ eV). The small Δ values can be interpreted as corresponding to the carrier excitation energy from the valence band to an impurity band (IB) formed within the bandgap, as discussed later. In the high temperature range above ~200 K, the slope of $\rho(T)$ becomes gentle. This should be due to the saturation of the IB. In the low-temperature range below ~120 K, the slope of $\rho(T)$ becomes gentle again. $\rho(T)$ in this temperature range can be explained by a 3D WAL-WL model combined with 3D electron-electron interaction (EEI), as described in detail later.

Previous studies have shown that $\rho(T)$ data of a series of $(Bi,Sb)_2(Se,Te)_3$ TIs generally show activated temperature dependence above about 100 K [8,10]. Here, the Δ values range from 20 to 60 meV, which are much smaller than the bandgap ($E_g = 0.2-0.3$ eV). Below the temperature range of the activated behavior, $\rho(T)$ has been shown to be better described by the mechanism of variable-range hopping (VRH).

Ren *et al.* [8] have argued the origin of such behaviors in relation with an IB within the bandgap, formed by acceptors. Here, the IB should consist of both extended and localized states because of a random distribution of the acceptors. At 0 K, the chemical potential is located within the IB. As temperature increases, the VRH conduction of localized carriers can take place alongside the conduction of extended carriers within the IB. At higher temperatures, electrons in the valence band can be thermally excited to the IB, and the conduction of the holes created at the top of the valence band becomes dominant. This should give the observed activated temperature dependence of $\rho(T)$ above 100 K. The activated temperature dependence observed for our samples, in which the excitation energies are much smaller than the bandgap, can be interpreted as arising from the same origin as in the $(Bi,Sb)_2(Se,Te)_3$ TIs. However, $\rho(T)$ data in our samples in the low-temperature range were found not to agree with the VRH conduction. Instead, they can

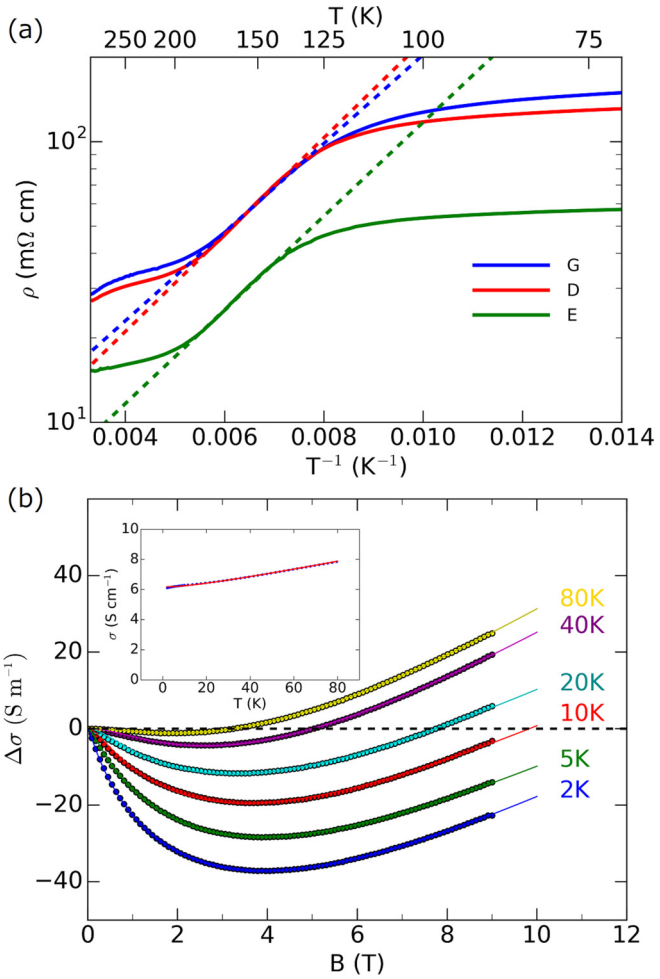

FIG. 7. (a) Arrhenius plots of $\rho(T)$ for the three most resistive samples (G, D, and E) in Fig. 4(a), where activated temperature dependence is seen in an intermediate temperature range around 150 K. The excitation energies evaluated are $\Delta = 31, 32$, and 34 meV for G, D, and E, respectively. (b) $\Delta\sigma(B)$ of sample D, measured at various temperatures, together with the fitting curves. $\sigma(T)$ of sample D and the corresponding fitting curve are shown in the inset.

be described well by a 3D WAL-WL model combined with 3D EEI. Below, we analyze our $\rho(T)$ and also MR data in the low-temperature range in terms of the model. Here, we begin with the MR data.

In Fig. 7(b), the MR curves of sample D in the temperature range 2−80 K in Fig. 6(b) are converted to magnetoconductivity (MC) [$\Delta\sigma(B) = \sigma(B) - \sigma(0)$] curves. On the basis of the 3D WAL-WL model, the quantum correction to MC is expressed as [30,31]

$$\Delta\sigma_{\mathrm{WAL-WL}}(B) = -\alpha\frac{e^2}{2\pi^2\hbar}\sqrt{\frac{eB}{\hbar}}\left\{\frac{1}{2}f_3\left(\frac{B}{B_\varphi}\right) - \frac{3}{2}f_3\left(\frac{B}{B_\varphi + (4/3)B_{\mathrm{SO}}}\right)\right\}, \quad (1)$$

where α is a prefactor, which is unity in the original expression, and B_φ and B_{SO} are characteristic fields related to the phase coherence length L_φ (relaxation time: τ_φ) and the spin orbit

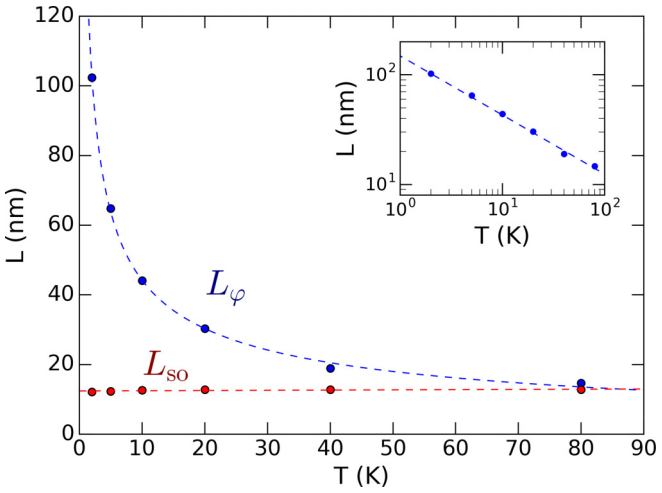

FIG. 8. Temperature dependence of the phase coherence length (L_φ) and the spin orbit flip length (L_{SO}). The log-log plot of L_φ is presented in the inset, where the data are fitted to the relation $L_\varphi \propto T^\alpha$ with $\alpha = -0.54$.

flip length L_{SO} (τ_{SO}):

$$B_\varphi = \frac{\hbar}{4eD\tau_\varphi} = \frac{\hbar}{4eL_\varphi^2},$$
$$B_{SO} = \frac{\hbar}{4eD\tau_{SO}} = \frac{\hbar}{4eL_{SO}^2}. \quad (2)$$

Here, D denotes the diffusion constant, and L_φ and τ_φ can often be approximated by the inelastic scattering length and time, respectively. $f_3(x)$ is defined as

$$f_3(x) = \sum_{N=0}^{\infty}\left\{2\left(\sqrt{N+1+\frac{1}{x}} - \sqrt{N+\frac{1}{x}}\right) - \frac{1}{\sqrt{N+\frac{1}{2}+\frac{1}{x}}}\right\}. \quad (3)$$

In Fig. 7(b), the MC curves are fitted to the theoretical $\Delta\sigma_{WAL-WL}(B)$ in Eq. (1) with three fitting parameters; α, L_φ, and L_{SO}. Here, the fitting curves agree quite well with the MC data. It should be noted that we also attempted to fit our data to the form, $\Delta\sigma(B) = \Delta\sigma_{WAL-WL}(B) + \Delta\sigma_{EEI}(B)$, where $\Delta\sigma_{EEI}(B)$ is the quantum correction due to EEI [31]:

$$\Delta\sigma_{EEI}(B) = -\frac{e^2}{4\pi^2\hbar}F_0\sqrt{\frac{k_BT}{2\hbar D}}g_3(x). \quad (4)$$

Here, F_0 is the screening factor, and the function $g_3(x)$ is given in the paper [31], where $x = \frac{g\mu_BB}{k_BT}$. As a result, we found that the EEI contribution is negligible for our data, i.e., $F_0 \approx 0$.

The α values obtained by the fittings in Fig. 7(b) are in the range 0.25−0.4, which are comparable to those previously evaluated for heavily doped semiconductors: 0.4−0.5 for n-Ge [32], 0.3−0.7 for n-GaAs [33,34], and 0.55 for n-InSb. [35] The obtained values of L_φ and L_{SO} are plotted against the temperature in Fig. 8. On one hand, L_{SO} (≈12 nm) is almost independent of the temperature. On the other hand, L_φ decreases rapidly with increasing temperature; we notice the form $L_\varphi \propto T^\alpha$ ($\alpha \approx -0.5$), as evidenced by the log-log plot in the inset of Fig. 8. At low temperatures, where $L_\varphi \gg L_{SO}$, WAL behavior in the low-B region is clearly observed in Fig. 7(b), which becomes less pronounced as L_φ approaches L_{SO} with increasing temperatures. At 80 K, where $L_\varphi \approx L_{SO}$, the WAL behavior has vanished almost completely and only WL behavior is observed. The relation $L_\varphi \propto T^{-0.5}$ shown in Fig. 8 leads to $\tau_\varphi \propto T^{-1}$, which has been previously reported for heavily doped semiconductors such as n-Ge [32] and n-GaAs [34,36]. Isawa [37] theoretically derived a formula for τ_φ, which consists of two terms that are proportional to T^{-1} and $T^{-\frac{3}{2}}$; a transition from $\tau_\varphi \propto T^{-1}$ at low temperatures to $\tau_\varphi \propto T^{-\frac{3}{2}}$ at high temperatures is expected. The low-temperature part of this theoretical τ_φ may be observed in our measurements.

The temperature dependences of the WAL-WL and EEI quantum corrections to conductivity, $\Delta\sigma_{WAL-WL}(T)$ [38] and $\Delta\sigma_{EEI}(T)$ [31], respectively are given as

$$\Delta\sigma_{WAL-WL}(T) = \frac{e^2}{2\pi^2\hbar L_{SO}}(3\sqrt{t+1} - \sqrt{t})$$
$$\text{where } t = \tau_{SO}/(4\tau_\varphi) = L_{SO}^2/\left(4L_\varphi^2\right), \quad (5)$$

$$\Delta\sigma_{EEI}(T) = \frac{0.23e^2}{\pi^2\hbar}\left(\frac{4}{3} - \frac{3F_0}{2}\right)\sqrt{\frac{k_BT}{\hbar D}}. \quad (6)$$

We have attempted to fit the $\sigma(T)$ data of sample D in the low-temperature range below 80 K to the theoretical $\sigma(T) = \sigma_0 + \Delta\sigma_{WAL-WL}(T) + \Delta\sigma_{EEI}(T)$. Here, L_φ and L_{SO} in Fig. 8 are used, and $F_0 = 0$ is assumed, leaving two adjusting parameters: σ_0 and D. The result of the fitting is presented in the inset of Fig. 7(b), where the fitting curve agrees well with the experimental $\sigma(T)$. Here, the obtained diffusion constant is $D = 1.04 \times 10^{-3}\ \mathrm{m^2 s^{-1}}$, which is approximately the same as that reported for a Bi_2Se_3 TI. [39]

From all the above analyses, we can conclude that both $\rho(T)$ [$\Delta\sigma(T)$] and $\rho(B)$ [$\Delta\sigma(B)$] data in the low-temperature range below 80 K agree well with the 3D WAL-WL model combined with the 3D EEI. These can be interpreted as the bulk conduction of carriers subjected to disorder scatterings in the IB formed within the bandgap. As mentioned in Sec. III B, the surface contribution to the total conductance in our samples is considerably small (2–4%) due to a relatively large sample thickness (0.14 mm). This is consistent with the fact that our $\rho(T)$ and $\rho(B)$ data can almost entirely be attributed to bulk conduction. The surface contribution can be increased simply by reducing sample thickness. Transport measurements for much thinner samples are now in progress to investigate the transport properties characteristic of 2D surface Dirac fermions in the present system.

IV. SUMMARY

A series of $Pb(Bi_{1-x}Sb_x)_2Te_4$ crystals, which are topological insulators with the invariants (1;111), was fabricated, and their transport properties were studied systematically, aiming at realizing enhanced bulk insulation in this system. First, $Pb(Bi_{1-x}Sb_x)_2Te_4$ crystals with various x were grown by the Bridgman method. EPMA and XRD experiments showed that,

based on the constitution of the phases, the grown rod can be divided into three different regions: bottom, middle, and top regions. The bottom region consisted of a dendritic PbTe phase embedded in a matrix of the $Pb(Bi,Sb)_2Te_4$ phase, the middle region consisted entirely of the $Pb(Bi,Sb)_2Te_4$ phase, whereas the top region had a lamellar structure of the $Pb(Bi,Sb)_2Te_4$ and $(Bi,Sb)_2Te_3$ phases.

From the middle region, millimeter-sized single crystals of $Pb(Bi_{1-x}Sb_x)_2Te_4$ phase were taken out by breaking the ingot along the cleavage planes for electrical transport measurements. Hall-effect measurements showed that the n- to p-type transition in bulk conduction occurred at $x \approx 0.80$. Semiconducting behavior with a negative temperature coefficient of resistivity and resistivity values as high as 180 mΩ cm at 2 K were observed around the transition composition. The carrier density was evaluated to be 1.7×10^{18} cm^{-3} at 2 K. The resistivity and the carrier density of the semiconducting samples were found to be higher and lower than those previously reported for the ternary $PbBi_2Te_4$ and $PbSb_2Te_4$ phases, respectively, by two to three orders of magnitude. In view of the previous studies on the $(Bi,Sb)_2(Se,Te)_3$ TIs, our crystals with resistivity of $\sim$180 mΩ cm are expected to be available for the study of surface transport properties.

The temperature and magnetic-field dependences of resistivity in a low temperature range below about 80 K agree well with a 3D WAL-WL model combined with 3D EEI. These can be interpreted as the bulk conduction of carriers in an IB formed within the bandgap. In an intermediate temperature range between around 150 K, an activated temperature dependence of resistivity was observed, attributable to thermal excitation of electrons in the valence band to the IB. Above about 200 K, the temperature dependence of resistivity became weak, indicating the saturation of the IB.

ACKNOWLEDGMENTS

The resistivity measurements were conducted using the facilities of the Cryogenic Research Center, The University of Tokyo. This work was financially supported by JSPS KAKENHI (Grant No. 16K14371) and Hitachi Metals - Materials Science Foundation.

[1] M. Z. Hasan and C. L. Kane, Rev. Mod. Phys. **82**, 3045 (2010).
[2] M. König, S. Wiedmann, C. Brüne, A. Roth, H. Buhmann, L. W. Molenkamp, X.-L. Qi, and S.-C. Zhang, Science **318**, 766 (2007).
[3] D. Hsieh, D. Qian, L. Wray, Y. Xia, Y. S. Hor, R. J. Cava, and M. Z. Hasan, Nature (London) **452**, 970 (2008).
[4] D. O. Scanlon, P. D. C. King, R. P. Singh, A. de la Torre, S. M. Walker, G. Balakrishnan, F. Baumberger, and C. R. A. Catlow, Adv. Mater. **24**, 2154 (2012).
[5] Y. Ando, J. Phys. Soc. Jpn. **82**, 102001 (2013).
[6] D. Hsieh, Y. Xia, D. Qian, L. Wray, J. H. Dil, F. Meier, J. Osterwalder, L. Patthey, J. G. Checkelsky, N. P. Ong, A. V. Fedorov, H. Lin, A. Bansil, D. Grauer, Y. S. Hor, R. J. Cava, and M. Z. Hasan, Nature (London) **460**, 1101 (2009).
[7] D. X. Qu, Y. S. Hor, J. Xiong, R. J. Cava, and N. P. Ong. Science **329**, 821 (2010).
[8] Z. Ren, A. A. Taskin, S. Sasaki, K. Segawa, and Y. Ando, Phys. Rev. B **82**, 241306 (2010)
[9] J. Zhang, C.-Z. Chang, Z. Zhang, J. Wen, X. Feng, K. Li, M. Liu, K. He, L. Wang, X. Chen, Q.-K. Xue, X. Ma, and Y. Wang, Nat. Commun. **2**, 574 (2011).
[10] Z. Ren, A. A. Taskin, S. Sasaki, K. Segawa, and Y. Ando, Phys. Rev. B **84**, 165311 (2011).
[11] Z. Ren, A. A. Taskin, S. Sasaki, K. Segawa, and Y. Ando, Phys. Rev. B **85**, 155301 (2012).
[12] S. K. Kushwaha, I. Pletikosic, T. Liang, A. Gyenis, S. H. Lapidus, Y. Tian, H. Zhao, K. S. Burch, J. Lin, W. Wang, H. Ji, A. V. Fedorov, A. Yazdani, N. P. Ong, T. Valla, and R. J. Cava, Nat. Commun. **7**, 11456 (2016).
[13] A. A. Taskin, Z. Ren, S. Sasaki, K. Segawa, and Y. Ando, Phys. Rev. Lett. **107**, 016801 (2011).
[14] H. Jin, J.-H. Song, A. J. Freeman, and M. G. Kanatzidis, Phys. Rev. B **83**, 041202 (2011).
[15] T. V. Menshchikova, S. V. Eremeev, Y. M. Koroteev, V. M. Kuznetsov, and E. V. Chulkov, JETP Lett. **93**, 15 (2011).
[16] S. V. Eremeev, G. Landolt, T. V. Menshchikova, B. Slomski, Y. M. Koroteev, Z. S. Aliev, M. B. Babanly, J. Henk, A. Ernst, L. Patthey, A. Eich, A. A. Khajetoorians, J. Hagemeister, O. Pietzsch, J. Wiebe, R. Wiesendanger, P. M. Echenique, S. S. Tsirkin, I. R. Amiraslanov, J. H. Dil, and E. V. Chulkov, Nat. Commun. **3**, 635 (2012).
[17] T. V. Menshchikova, S. V. Eremeev, and E. V. Chulkov, Appl. Surf. Sci. **267**, 1 (2013).
[18] A. Bansil, H. Lin, and T. Das, Rev. Mod. Phys. **88**, 021004 (2016).
[19] S. Souma, K. Eto, M. Nomura, K. Nakayama, T. Sato, T. Takahashi, K. Segawa, and Y. Ando, Phys. Rev. Lett. **108**, 116801 (2012).
[20] K. Kuroda, H. Miyahara, M. Ye, S. V. Eremeev, Y. M. Koroteev, E. E. Krasovskii, E. V. Chulkov, S. Hiramoto, C. Moriyoshi, Y. Kuroiwa, K. Miyamoto, T. Okuda, M. Arita, K. Shimada, H. Namatame, M. Taniguchi, Y. Ueda, and A. Kimura, Phys. Rev. Lett. **108**, 206803 (2012).
[21] L. Fu, Phys. Rev. Lett. **103**, 266801 (2009).
[22] R.-J. Slager, A. Mesaros, V. Juricic, and J. Zaanen, Nat. Phys. **9**, 98 (2013).
[23] Y. Ran, Y. Zhang, and A. Vishwanath, Nat. Phys. **5**, 298 (2009).
[24] R.-J. Slager, A. Mesaros, V. Juricic, and J. Zaanen, Phys. Rev. B **90**, 241403(R) (2014).
[25] O.A. Tretiakov, Ar. Abanov, S. Murakami, and J. Sinova, Appl. Phys. Lett. **97**, 073108 (2010).
[26] H. Hamasaki, Y. Tokumoto, and K. Edagawa, Appl. Phys. Lett. **110**, 092105 (2017).
[27] L. Pan, J. Li, D. Berardan, and N. Dragoe, J. Solid State Chem. **225**, 168 (2015).
[28] L. E. Shelimova, O. G. Karpinskii, T. E. Svechnikova, E. S. Avilov, M. A. Kretova, and V. S. Zemskov, Inorg. Mater. **40**, 1264 (2004).
[29] L. E. Shelimova, O. G. Karpinskii, T. E. Svechnikova, I. Y. Nikhezina, E. S. Avilov, M. A. Kretova, and V. S. Zemskov, Inorg. Mater. **44**, 371 (2008).

[30] A. Kawabata, J. Phys. Soc. Jpn. **49**, 628 (1980).
[31] P. A. Lee and T. V. Ramakrishnan, Rev. Mod. Phys. **57**, 287 (1985).
[32] T. A. Polyanskaya and I. I. Saidashev, JETP Lett. **34**, 361 (1981).
[33] O. V. Emel'yanenko, T. S. Lagunova, and T. A. Polyanskaya, JETP Lett. **36**, 246 (1982).
[34] S. Morita, N. Mikoshiba, Y. Koike, T. Fukase, M. Kitagawa, and S. Ishida, J. Phys. Soc. Jpn. **53**, 2185 (1984).
[35] R. C. Dynes, T. H. Geballe, G. W. Hull, Jr., and J. P. Garno, Phys. Rev. B **27**, 5188 (1983).
[36] B. Capoen, G. Biskupski, and A. Briggs, J. Phys.: Condens. Matter **5**, 2545 (1993).
[37] Y. Isawa, J. Phys. Soc. Jpn. **53**, 2865 (1984).
[38] H. Fukuyama and K. Hoshino, J. Phys. Soc. Jpn. **50**, 2131 (1981).
[39] Y. Zhao, H. Liu, X. Guo, Y. Jiang, Y. Sun, H. Wang, Y. Wang, H.-D. Li, M.-H. Xie, X.-C. Xie, and J. Wang, Nano Lett. **14**, 5244 (2014).